

Interrelation of elasticity and thermal bath in nanotube cantilevers

S. Tepsic,¹ G. Gruber,¹ C. B. Møller,¹ C. Magén,^{2,3} P. Belardinelli,⁴
E. R. Hernández,⁵ F. Alijani,⁶ P. Verlot,⁷ and A. Bachtold¹

¹*ICFO - Institut De Ciències Fotoniques, The Barcelona Institute of Science and Technology, 08860 Castelldefels (Barcelona), Spain*

²*Instituto de Nanociencia y Materiales de Aragón (INMA), CSIC-Universidad de Zaragoza, 50009 Zaragoza, Spain*

³*Laboratorio de Microscopías Avanzadas (LMA), Universidad de Zaragoza, 50018 Zaragoza, Spain*

⁴*DICEA, Polytechnic University of Marche, 60131 Ancona, Italy*

⁵*Instituto de Ciencia de Materiales de Madrid (ICMM-CSIC), 28049 Madrid, Spain*

⁶*Department of Precision and Microsystems Engineering, 3ME, Mekelweg 2, (2628 CD) Delft, The Netherlands*

⁷*School of Physics and Astronomy - The University of Nottingham, University Park, Nottingham NG7 2RD, United Kingdom*

We report the first study on the thermal behaviour of the stiffness of individual carbon nanotubes, which is achieved by measuring the resonance frequency of their fundamental mechanical bending modes. We observe a reduction of the Young's modulus over a large temperature range with a slope $-(173 \pm 65)$ ppm/K in its relative shift. These findings are reproduced by two different theoretical models based on the thermal dynamics of the lattice. These results reveal how the measured fundamental bending modes depend on the phonons in the nanotube via the Young's modulus. An alternative description based on the coupling between the measured mechanical modes and the phonon thermal bath in the Akhiezer limit is discussed.

In engineering, thermoelasticity is central in determining the elastic limits of structures ranging from large scale spacecrafts [1] and nuclear plants [2] down to nano-structured systems. A rich underlying phenomenology emerges for small structures, including dissipation [3, 4], fluctuations [5, 6], and torque generation [7, 8], which are key to the development of state-of-the-art nano- and micro-electromechanical technologies [9, 10]. Thermoelasticity has also been used with success in condensed matter physics, where thermal measurements of the stiffness unveil the phase transition of charge-density waves and superconductivity in transition metal dichalcogenides and high- T_c superconductors [11–13]. From a fundamental point of view, the thermal behaviour of the stiffness – quantified by the Young's modulus – emerges from the non-trivial interplay of the binding energy and the lattice dynamics. However, the effect of the thermal lattice dynamics on the stiffness has remained elusive in individual nanoscale systems due to experimental challenges related to manipulating and measuring such small objects.

In this work, we use the exquisite sensing capabilities of mechanical resonators based on nanoscale systems [14–29] to resolve the small effect associated with the thermal behaviour of their stiffness. Using the resonance frequency measured by optomechanical spectroscopy, we estimate the Young's modulus of micrometer-long nanotube cantilevers from room temperature down to a few Kelvins. These results agree with the temperature dependence of the resonance frequency predicted by molecular dynamics simulations, which take into account the lattice dynamics of the nanotube. Our measurements

are also consistent with the Young's modulus directly computed from a quasi-harmonic approximation of the free energy of the phonon modes. This work not only shows how the stiffness of an individual nanotube is related to its phonons, but it also highlights the role of the phonon thermal bath in nanotube cantilevers, which is a topic of importance in the field of nanomechanical resonators [14–29].

We use the single clamped resonator layout, where one end of the nanotube is attached to a silicon chip and the other end is free. This layout avoids prestress in the nanotube built-in during fabrication, in contrast to what may happen with the double clamped layout. As a result, the restoring force is given solely by the bending rigidity. This enables us to probe the Young's modulus Y by measuring the resonance frequency, $\omega_0 \propto \sqrt{Y}$ [32]. Such a resonance-based methodology is also employed in thermoelasticity studies on larger scale systems [11–13, 33].

We engineer a platinum particle at the free end of the nanotube, so that the resonator can be measured by scattering optomechanical spectroscopy (Fig. 1a) [31]. We grow the particle by focused electron beam-induced deposition [30]. Figure 1b shows a scanning electron microscopy image of device A. Transmission electron microscopy (TEM) indicates that nanotubes can be made from one to a few walls, with a median value of two walls (Supplementary Material, Sec. I [34]). The vibrations are detected by measuring the backscattered intensity from a 632 nm laser beam focused onto the particle. Figure 1c shows the optomechanical spectrum of device A. The resonance frequencies of the fundamental

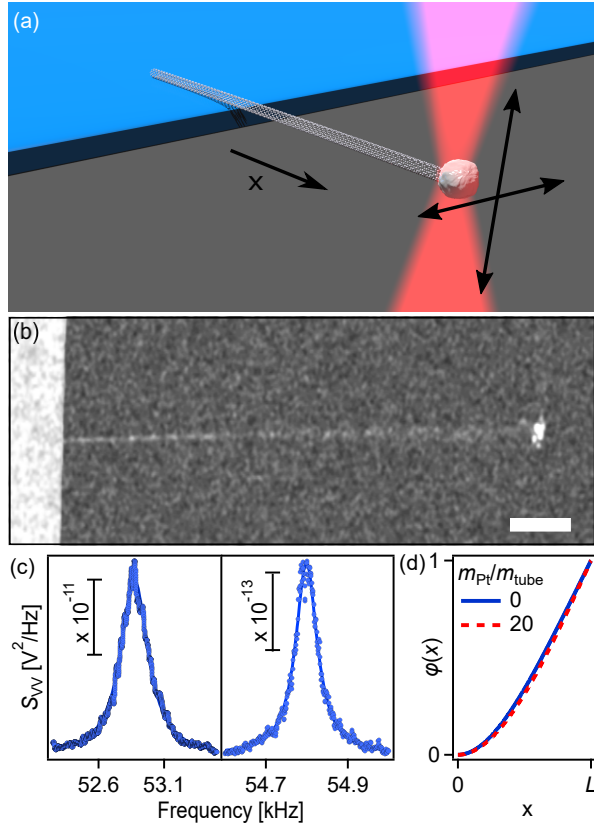


FIG. 1. (a) Schematic of the experimental setup. The sample is placed at the waist of a strongly focused beam of a He-Ne laser. The scattered light (not shown) is collected in reflection by means of an optical circulator and further sent on an avalanche photodetector. The two double arrows represent the polarization of the fundamental mode doublet. (b) Device A imaged by scanning electron microscopy after the deposition of a platinum nanoparticle; the scale bar is $1\mu\text{m}$ [30]. (c) Power spectra of the optical reflection from device A showing the resonance of the thermal motion of the fundamental mode doublet at 300 K. The two spectra are recorded using different positions of the nanotube in the laser waist to enhance the signal [31]. (d) Calculated profile $\varphi(x)$ of the fundamental mode shape along the nanotube axis estimated for two different platinum particle masses normalized by the nanotube mass.

modes polarized in perpendicular directions are about 52.9 kHz and 54.8 kHz. The platinum particle does not affect the restoring force nor the eigenmode shape of the two fundamental modes (Fig. 1d), in contrast to what happens for higher frequency modes (Supplementary Material, Sec. II [34]). In this work we use low laser power so that the resonance frequency is not affected by absorption heating and optical backaction [31].

We quantify $Y = (1.06 \pm 0.28)$ TPa at room temperature from six devices by combining thermal motion variance measurement and TEM imaging; the advantage of this method is that it does not rely on

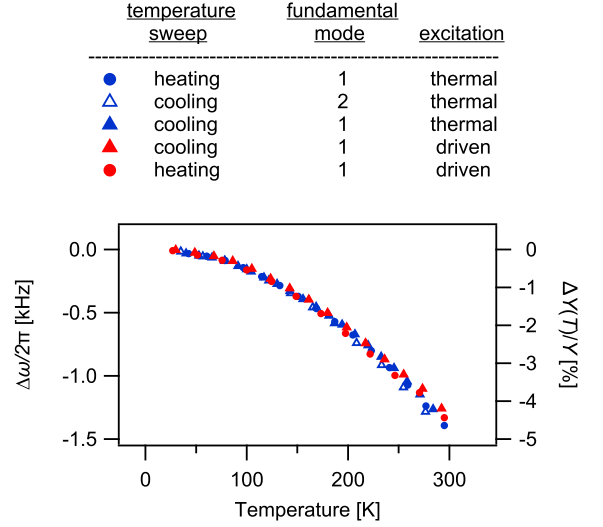


FIG. 2. Resonance frequency and relative change of the Young's modulus of device A as a function of cryostat temperature. The legend indicates the direction of the temperature sweep (cooling or heating), which fundamental mode is measured, and whether the detected vibrations are thermal or driven with a piezo-actuator.

the cantilever mass (Supplementary Material, Sec. III [34]). The estimated Young's modulus is similar to previously predicted and measured values [53–58]. This indicates that the contamination adsorbed on the nanotube surface has little contribution to the stiffness of the nanotube. The contamination, which is localized along some portions of nanotubes as observed by TEM, presumably consists of hydrocarbons adsorbed during their exposure to air and the particle growth. The typical stiffness reported for such amorphous material is comparatively low $Y \approx (50 - 300)$ GPa [59].

Figure 2 shows the variation of the resonance frequency of device A when sweeping the temperature T . The variation is remarkably similar for both fundamental modes, independent of the temperature sweep direction and of whether the motion is thermal or driven with a piezo-actuator. This variation of the resonance frequency $\omega_0 = \sqrt{k/m}$ is associated to the change of the spring constant k , which is linearly proportional to Y in the single clamped layout. We extract the relative shift of the Young's modulus from the relation $\frac{\Delta Y(T)}{Y(T_{min})} = 2 \frac{\Delta \omega_0(T)}{\omega_0(T_{min})}$, where T_{min} is the lowest temperature at which we record the vibrations. Figure 3a shows the measurements of nine different devices. They all feature the same trend with a reduction of the Young's modulus when increasing temperature. The dependence is essentially linear above about 100 K; the slope averaged over devices is $\Delta Y(T)/Y \cdot 1/T = -(173 \pm 65)$ ppm/K. These measurements are related to neither the mass

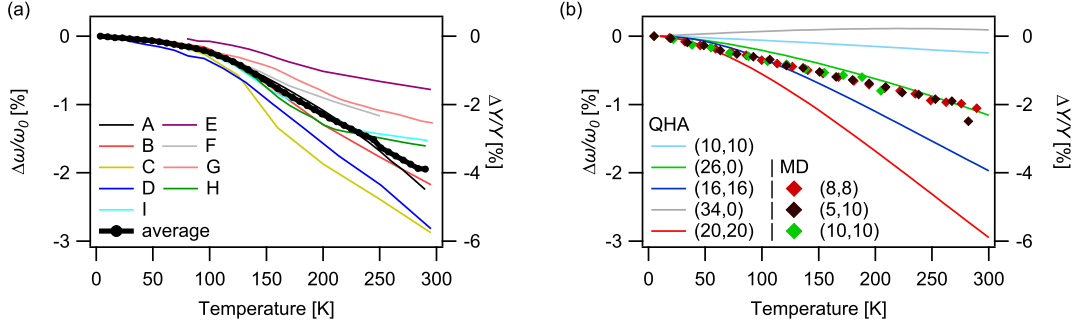


FIG. 3. Comparison of the relative change of the resonance frequency and the Young's modulus between experiment (a) and theory (b) for different nanotubes. The theoretical results are obtained for different nanotube chiralities with either molecular dynamics (MD) simulations or quasi-harmonic approximation (QHA) calculations. The MD simulations and the QHA calculations quantify $\Delta\omega_0/\omega_0$ and $\Delta Y/Y$, respectively.

adsorbed on the nanotube nor the diffusion of adsorbed atoms along the nanotube nor the thermal expansion of the nanotube nor the combination of the Duffing nonlinearity and the thermal motion, as shown in Sec. IV of Supplementary Material [34].

These measurements can be captured by molecular dynamics (MD) simulations of the nanotube cantilever dynamics. The temperature dependence of the resonance frequencies of the lowest energy bending modes obtained from the MD simulations behave in the same way as those we measure (Figs. 3a,b). The associated slope estimated for different nanotube chiralities leads to $\Delta Y(T)/Y \cdot 1/T = -(79 \pm 6)$ ppm/K, which is rather similar to the measured value. This suggests that the thermal behaviour of the Young's modulus in our measurements is related to the lattice dynamics of nanotubes.

We employ a second method to directly compute the Young's modulus from the energy dispersion of the nanotube phonon modes. For this, we evaluate the free energy $F(T, \epsilon)$ of the phonon modes at T and strain ϵ with the quasi-harmonic approximation, yielding

$$Y(T) = \frac{1}{V_0(T)} \left(\frac{\partial^2 F(T, \epsilon)}{\partial \epsilon^2} \right)_{\epsilon=0},$$

where $V_0(T)$ is the equilibrium volume at this temperature. The resulting $Y(T)$ dependence is also consistent with the measurements (Figs. 3a,b). The slope for different chiralities is $\Delta Y(T)/Y \cdot 1/T = -(104 \pm 102)$ ppm/K. The variation of the slope is larger than that obtained with molecular dynamics; this difference may be due to the infinite nanotube length and the purely linear vibrational dynamics considered in the quasi-harmonic approximation method, while the lengths in the molecular dynamics simulations are much shorter, that is, less than 40 nm. Overall, the experimental findings are fairly consistent with both models considering the typical differences between the values of Y of nanotubes obtained with different experimental and theoretical

methods [53–58]. Both theoretical models are described in the Supplementary Material (Secs. V and VI) [34].

These results show how the measured fundamental mechanical modes are linked to phonons via the Young's modulus. An alternative way to describe this link is to consider the coupling of the measured mechanical modes with the thermal bath made of the phonons of the nanotube. In other words, the measured T dependence of ω_0 is related to the phonon thermal bath. It is likely that the phonon thermal bath in our experiments operate in the Akhiezer limit [60]. Over the temperature range that we measure, the phonon modes in nanotubes with energy $\hbar\omega_k$ similar to $k_B T$ have decay rates $1/\tau_k$ larger than ω_0 , since $\tau_k \approx 10$ ns was measured for breathing modes at $T = 5$ K [61] and we estimate τ_k to be typically in the 10 – 1000 ns range for the longitudinal and twist modes [62] (Sec. VII of Supplementary Material [34]). (The estimation of τ_k for high-energy bending modes is complicated and beyond the scope of this work.) This sets the Akhiezer limit $\omega_0 \tau_k \ll 1$ at least for the breathing, longitudinal, and twist modes [63]. It involves three-phonon processes, where one vibration quantum of the measured mode is absorbed together with the absorption and the emission of high-energy phonons with frequencies ω_k and $\omega_{k'}$, respectively. The sizeable decay rates of the high-energy phonons lead to uncertainty in their energy. This lifts to some extent the restriction associated with the energy conservation of the three-phonon process, $\omega_0 = \omega_k - \omega_{k'}$, which holds in the Landau-Rumer limit when $\omega_0 \tau_k \gg 1$. For this reason, the resonance frequency reduction and the relaxation in the Akhiezer limit are expected to be larger than that in the Landau-Rumer limit over the studied temperature range. The thermoelastic limit [4] does not apply for nanotubes, since the model relies on phonons that locally reach thermal equilibrium at different temperatures on the two sides of the beam cross-section, which is not realistic for such narrow resonators.

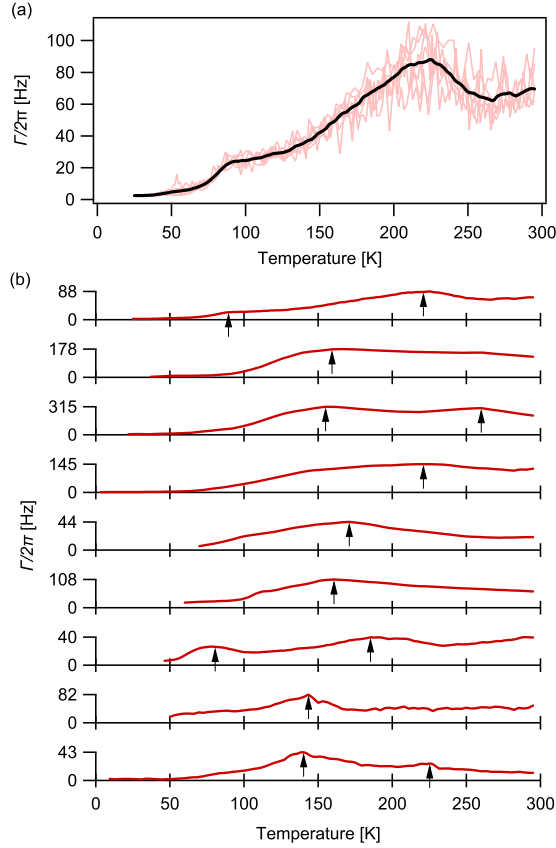


FIG. 4. (a) Temperature dependence of the mechanical linewidth for device A. The black line is the average of different temperature traces (red lines). (b) Temperature dependence of the linewidth for all the measured nanotubes, from device A at the top to device I at the bottom; the associated resonance frequencies are 54 kHz, 96 kHz, 194 kHz, 77 kHz, 57 kHz, 108 kHz, 44 kHz, 58 kHz, 48 kHz. The arrows indicate peaks in dissipation.

It is expected that the phonon thermal bath significantly contributes to the measured dissipation via the Akhiezer relaxation, since a thermal bath results in a resonance frequency reduction as well as dissipation, both of them being related through the Kramers–Kronig relations [64]. Figures 4a,b show the measured temperature dependence of the mechanical linewidth of the different measured devices. The measurements feature one or two peaks of dissipation at some specific temperatures. These observed peaks could arise from the Akhiezer relaxation. The Akhiezer dissipation rate depends in a complicated way on the number of phonon modes with energy $\hbar\omega_k \lesssim k_B T$, their population, and their decay rate [63]. The temperature dependence of the Akhiezer dissipation rate could feature one or more peaks in dissipation, especially since the phonon density of states varies up and down as a function of energy [62, 65] and the temperature behaviour of

the decay rate changes for different phonon modes. In addition, the dissipation peaks could emerge at different temperatures for different nanotube chiralities, since the phonon energy dispersion is chirality dependent. The measured peaks in dissipation cannot be described by the model that is used in the literature [66, 67] to quantify dissipation due to defects. See Secs. VIII and IX of Supplementary Material for further discussion on the Akhiezer dissipation and dissipation due to defects [34].

In conclusion, we report the first experimental study of the temperature dependence of the Young’s modulus of a nanoscale system. The measurements are consistent with theoretical predictions based on the nanotube lattice dynamics. This indicates that the phonon thermal bath plays an important role in the dynamics of nanotube cantilevers, including thermal vibrational noise, dissipation, and resonance frequency reduction. Further theoretical work is needed to compute the Akhiezer relaxation in nanotubes beyond the models used so far, where a single decay rate is employed for all the high-frequency phonon modes [67–69]. This may be achieved with a microscopic theory [63] taking into account the phonon energy dispersion [65] and the energy decay of high-frequency phonons [62]. It will be interesting to see whether such a model leads to dissipation peaks at specific temperatures as observed in our work.

We thank Mark Dykman and Andrew Fefferman for enlightening discussions. This work is supported by ERC advanced (grant number 692876), ERC PoC (grant number 862149), Marie Skłodowska-Curie PROBIST (grant number 754510), the Cellex Foundation, the CERCA Programme, AGAUR (grant number 2017SGR1664), Severo Ochoa (grant number SEV-2015-0522), MICINN (grant number RTI2018-097953-B-I00 and PGC2018-096955-B-C44), the Fondo Europeo de Desarrollo Regional, the grant MAT2017-82970-C2-2-R of Spanish MINECO and the project E13_17R from Aragon Regional Government (Construyendo Europa desde Aragón). F.A. acknowledges support from European Research Council (ERC) starting grant number 802093.

-
- [1] E. A. Thornton, *Thermal structures for aerospace applications* (American Institute of Aeronautics and Astronautics, 1996).
 - [2] Z. Zudans, T. C. Yen, and W. H. Steigelmann, *Thermal stress techniques in the nuclear industry* (American Elsevier Publishing Company, 1965).
 - [3] C. Zener, *Phys. Rev.* **53**, 90 (1938).
 - [4] R. Lifshitz and M. L. Roukes, *Phys. Rev. B* **61**, 5600 (2000).
 - [5] R. Kubo, *Rep Prog Phys* **29**, 255 (1966).
 - [6] A. N. Cleland and M. L. Roukes, *J Appl Phys* **92**, 2758

- (2002).
- [7] W. Fang, H.-C. Tsai, and C.-Y. Lo, *Sensors and Actuators A: Physical* **77**, 21 (1999).
 - [8] M. Murozono and S. Sumi, *Journal of Intelligent Material Systems and Structures* **5**, 21 (1994).
 - [9] P. R. Saulson, *Phys. Rev. D* **42**, 2437 (1990).
 - [10] T. R. Albrecht, P. Grütter, D. Horne, and D. Rugar, *J Appl Phys* **69**, 668 (1991).
 - [11] M. Barmatz, L. R. Testardi, and F. J. Di Salvo, *Phys. Rev. B* **12**, 4367 (1975).
 - [12] J. W. Brill and W. Roark, *Phys. Rev. Lett.* **53**, 846 (1984).
 - [13] S. Hoen, L. C. Bourne, C. M. Kim, and A. Zettl, *Phys. Rev. B* **38**, 11949 (1988).
 - [14] H.-Y. Chiu, P. Hung, H. W. C. Postma, and M. Bockrath, *Nano Lett* **8**, 4342 (2008).
 - [15] E. Gil-Santos, D. Ramos, J. Martínez, M. Fernández-Regúlez, R. García, A. San Paulo, M. Calleja, and J. Tamayo, *Nature Nanotechnology* **5**, 641 (2010).
 - [16] J. Chaste, A. Eichler, J. Moser, G. Ceballos, R. Rurali, and A. Bachtold, *Nat Nano* **7**, 301 (2012).
 - [17] J. Moser, J. Güttinger, A. Eichler, M. J. Esplandiú, D. E. Liu, M. I. Dykman, and A. Bachtold, *Nature Nanotechnology* **8**, 493 (2013).
 - [18] I. Yeo, P.-L. de Assis, A. Glappe, E. Dupont-Ferrier, P. Verlot, N. S. Malik, E. Dupuy, J. Claudon, J.-M. Gérard, A. Auffèves, G. Nogues, S. Seidelin, J.-P. Poizat, O. Arcizet, and M. Richard, *Nature Nanotechnology* **9**, 106 (2013).
 - [19] A. Siria, T. Barois, K. Vilella, S. Perisanu, A. Ayari, D. Guillot, S. Purcell, and P. Poncharal, *Nano Lett* **12**, 3551 (2012).
 - [20] R. M. Cole, G. A. Brawley, V. P. Adiga, R. De Alba, J. M. Parpia, B. Ilic, H. G. Craighead, and W. P. Bowen, *Phys. Rev. Applied* **3**, 024004 (2015).
 - [21] P. Weber, J. Güttinger, A. Noury, J. Vergara-Cruz, and A. Bachtold, *Nat. Commun.* **7**, 12496 (2016).
 - [22] L. M. de Lepinay, B. Pigeau, B. Besga, P. Vincent, P. Poncharal, and O. Arcizet, *Nature Nanotechnology* **12**, 156 (2016).
 - [23] N. Rossi, F. R. Braakman, D. Cadeddu, D. Vasyukov, G. Tutuncuoglu, A. Fontcuberta i Morral, and M. Poggio, *Nature Nanotechnology* **12**, 150 (2016).
 - [24] R. J. Dolleman, S. Hourri, D. Davidovikj, S. J. Cartamil-Bueno, Y. M. Blanter, H. S. J. van der Zant, and P. G. Steeneken, *PRB* **96**, 165421 (2017).
 - [25] S. L. de Bonis, C. Urgell, W. Yang, C. Samanta, A. Noury, J. Vergara-Cruz, Q. Dong, Y. Jin, and A. Bachtold, *Nano Lett.* **18**, 5324 (2018).
 - [26] A. Blaikie, D. Miller, and B. J. Aleman, *Nature Communications* **10**, 4726 (2019).
 - [27] N. Rossi, B. Gross, F. Dirnberger, D. Bougeard, and M. Poggio, *Nano Lett.* **19**, 930 (2019).
 - [28] P. Sahafi, W. Rose, A. Jordan, B. Yager, M. Piscitelli, and R. Budakian, *Nano Lett.* **20**, 218 (2020).
 - [29] F. Rogliano, B. Besga, A. Reigue, L. M. de Lepinay, P. Heringlake, C. Gouriou, E. Eyraud, W. Wernsdorfer, B. Pigeau, and O. Arcizet, arXiv preprint arXiv:2009.02912 (2020).
 - [30] G. Gruber, C. Urgell, A. Tavernarakis, A. Stavrinadis, S. Tepsic, C. Magen, S. Sangiao, J. M. De Teresa, P. Verlot, and A. Bachtold, *Nano letters* **19**, 6987 (2019).
 - [31] A. Tavernarakis, A. Stavrinadis, A. Nowak, I. Tsioutsios, A. Bachtold, and P. Verlot, *Nature Communications* **9**, 662 (2018).
 - [32] R. Lifshitz and M. C. Cross, in *Reviews of Nonlinear Dynamics and Complexity*, edited by H. G. Schuster (Wiley, Weinheim, 2008) pp. 1–52.
 - [33] J. B. Wachtman, W. E. Tefft, D. G. Lam, and C. S. Apstein, *Phys. Rev.* **122**, 1754 (1961).
 - [34] See Supplemental Material at [url] for additional discussion on device fabrication, mechanical eigenmodes, Young’s modulus, origin of the shift of the resonance frequency, theoretical modeling of nanotubes, phonon decay rates, Akhiezer dissipation and dissipation due to defects, which includes Refs. [35–52].
 - [35] I. Tsioutsios, A. Tavernarakis, J. Osmond, P. Verlot, and A. Bachtold, *Nano letters* **17**, 1748 (2017).
 - [36] B. Balachandran and E. Magrab, *Vibrations* (Nelson Education, 2008).
 - [37] J. Melcher, S. Hu, and A. Raman, *Applied Physics Letters* **91**, 053101 (2007).
 - [38] Z. Wang, J. Wei, P. Morse, J. G. Dash, O. E. Vilches, and D. H. Cobden, *Science* **327**, 552 (2010).
 - [39] Y. T. Yang, C. Callegari, X. L. Feng, and M. L. Roukes, *Nano Lett* **11**, 1753 (2011).
 - [40] A. Tavernarakis, J. Chaste, A. Eichler, G. Ceballos, M. C. Gordillo, J. Boronat, and A. Bachtold, *PRL* **112**, 196103 (2014).
 - [41] J. Atalaya, A. Isacson, and M. I. Dykman, *Phys. Rev. Lett.* **106**, 227202 (2011).
 - [42] S. Plimpton, P. Crozier, and A. Thompson, *Sandia National Laboratories* **18**, 43 (2007).
 - [43] J. Tersoff, *Phys. Rev. B* **37**, 6991 (1988).
 - [44] L. Lindsay and D. A. Broido, *Phys. Rev. B* **81**, 205441 (2010).
 - [45] C. Tang, W. Guo, and C. Chen, *Phys. Rev. B* **79**, 155436 (2009).
 - [46] B. I. Yakobson, C. J. Brabec, and J. Bernholc, *Phys. Rev. Lett.* **76**, 2511 (1996).
 - [47] R. Klessig and E. Polak, *SIAM Journal on Control* **10**, 524 (1972).
 - [48] D. J. Evans and B. L. Holian, *The Journal of Chemical Physics* **83**, 4069 (1985).
 - [49] B. Sajadi, S. Wahls, S. van Hemert, P. Belardinelli, P. G. Steeneken, and F. Alijani, *Journal of the Mechanics and Physics of Solids* **122**, 161 (2019).
 - [50] D. Porezag, F. Th., T. Köhler, G. Seifert, and R. Kraschner, *Physical Review B* **51**, 12947 (1995).
 - [51] D. Alfè, *Computer Physics Communications* **180**, 12947 (2009).
 - [52] R. Vacher, E. Courtens, and M. Foret, *Phys. Rev. B* **72**, 214205 (2005).
 - [53] M. M. J. Treacy, T. W. Ebbesen, and J. M. Gibson, *Nature* **381**, 678 (1996).
 - [54] A. Krishnan, E. Dujardin, T. W. Ebbesen, P. N. Yianilos, and M. M. J. Treacy, *Physical Review B* **58**, 14013 (1998).
 - [55] J.-P. Salvetat, G. Briggs, J.-M. Bonard, R. Bacsá, A. Kulik, T. Stöckli, N. Burnham, and L. Forró, *Physical Review Letters* **82**, 944 (1999).
 - [56] J. P. Lu, *Phys. Rev. Lett.* **79**, 1297 (1997).
 - [57] E. Hernández, C. Goze, P. Bernier, and A. Rubio, *Physical Review Letters* **80**, 4502 (1998).
 - [58] D. Sánchez-Portal, E. Artacho, J. M. Soler, A. Rubio, and P. Ordejón, *Physical Review B* **59**, 12678 (1999).
 - [59] J. Robertson, *Materials Science and Engineering: R: Reports* **37**, 129 (2002).

- [60] A. Akhiezer, Zh. Eksp. Teor. Fiz **8**, 1318 (1938).
- [61] B. J. LeRoy, S. G. Lemay, J. Kong, and C. Dekker, [Nature](#) **432**, 371 (2004).
- [62] A. De Martino, R. Egger, and A. O. Gogolin, [Phys. Rev. B](#) **79**, 205408 (2009).
- [63] J. Atalaya, T. W. Kenny, M. L. Roukes, and M. I. Dykman, [Phys. Rev. B](#) **94**, 195440 (2016).
- [64] L. Landau and E. Lifshitz, *Theory of Elasticity*, 3rd ed. (Butterworth-Heinemann Ltd., Oxford, 1986).
- [65] H. Suzuura and T. Ando, [Phys. Rev. B](#) **65**, 235412 (2002).
- [66] T. Faust, J. Rieger, M. J. Seitner, J. P. Kotthaus, and E. M. Weig, [Phys. Rev. B](#) **89**, 100102 (2014).
- [67] M. Hamoumi, P. E. Allain, W. Hease, E. Gil-Santos, L. Morgenroth, B. Gérard, A. Lemaitre, G. Leo, and I. Favero, [Phys. Rev. Lett.](#) **120**, 223601 (2018).
- [68] J. Rodriguez, S. A. Chandorkar, C. A. Watson, G. M. Glaze, C. H. Ahn, E. J. Ng, Y. Yang, and T. W. Kenny, [Sci. Rep.](#) **9**, 1 (2019).
- [69] S. S. Iyer and R. N. Candler, [Phys Rev Appl.](#) **5**, 034002 (2016).

Supplementary Material

I. DEVICE FABRICATION AND STRUCTURAL CHARACTERIZATION

The carbon nanotubes were grown on silicon substrates via chemical vapor deposition. A Zeiss Auriga scanning electron microscope (SEM) was used to select suitable nanotube cantilevers. The SEM is equipped with a gas injection system, which was used to deposit platinum particles at the apex of the nanotubes for their optomechanical functionalization [1, 2]. Figure 5(a) shows a pristine nanotube cantilever (device A). Figure 5(b) shows the same cantilever after the deposition of a Pt particle. The free end of the cantilever is blurred in the SEM images due to the thermally driven motion. The displacement profile was measured by a SEM line trace across the nanotube at the tip. Figure 5(c) shows the observed Gaussian distribution in the secondary electron current I_{SE} , as expected for thermal vibrations [3]. The displacement variance $\sigma^2 = (87.4 \text{ nm})^2$ was obtained from a fit of the data. The spring constant $k = 5.42 \times 10^{-7} \text{ N/m}$ was determined from the equipartition theorem $k = k_B T / \sigma^2$ where k_B is the Boltzmann constant and T is the temperature [3]. The mass of the deposited Pt particle was controlled during its growth by monitoring the mechanical resonance frequency of the lowest flexural mode of the nanotube; the thermal vibrations were measured by pointing the electron beam onto the apex of the nanotube in spot mode while recording the noise of I_{SE} [2]. The initial effective mass of the nanotube was $m_0^* = 243 \text{ ag}$ and the mass of the deposited particle visible in Fig. 5(b) was $m_{Pt} = (3.6 \pm 1.1) \text{ fg}$. All discussed samples were fabricated as described above. The mechanical properties of the samples that were optomechanically characterized at low temperature (devices A-I) are summarized in Table I.

We performed high-resolution transmission electron microscopy (HRTEM) to assess the microscopic structure of nanotube cantilevers. The samples were fabricated on silicon aperture windows using the identical procedure as outlined above. HRTEM imaging was conducted using a Thermo Fisher Titan Cube 60-300, equipped with an image aberration corrector CETCOR from CEOS. The microscope was operated at 80 kV to minimize beam damage and

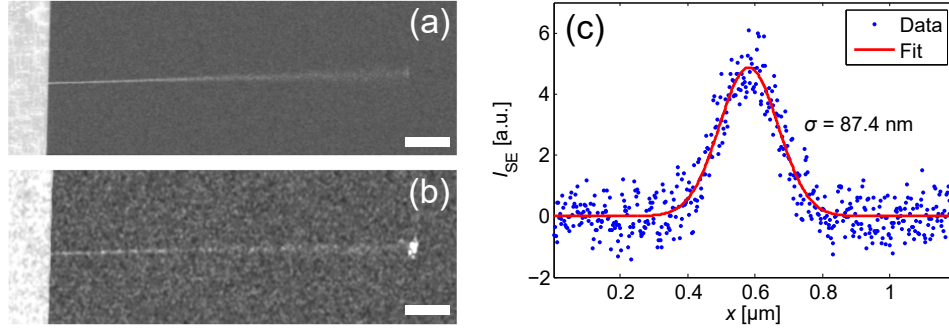


FIG. 5. Device A imaged by SEM (a) before and (b) after deposition of a Pt nanoparticle; the scale bars are $1 \mu\text{m}$. (c) Secondary electron signal I_{SE} across the apex of the nanotube; from a Gaussian fit the displacement variance $\sigma^2 = (87.4 \text{ nm})^2$ is determined.

TABLE I. Mechanical properties of the nanotube cantilever devices discussed in the main text. These include the length l , the standard deviation of the thermal displacement σ , the spring constant k , and the mass ratio m^* between the Pt particle and the nanotube as defined in Supplementary Section II.

Device	l (μm)	σ (nm)	k (N/m)	m^*
A	8.2	87.4	5.42×10^{-7}	3.7
B	6.5	22.8	7.92×10^{-6}	4.6
C	2.4	16.0	1.64×10^{-5}	83.0
D	7.8	55.8	1.33×10^{-6}	5.5
E	10.0	44.2	2.10×10^{-6}	4.6
F	5.0	34.9	3.39×10^{-6}	8.8
G	5.2	80.1	6.46×10^{-7}	18.3
H	4.6	73.5	7.63×10^{-7}	60.9
I	11.9	90.0	5.11×10^{-7}	3.7

achieve a spatial resolution below 1.4 \AA . Figure 6 shows atomically resolved images obtained for different devices near the clamping point where the thermal displacement is negligible. The devices shown are a single wall device, a seven wall device, and a triple wall device. The latter device was also characterized optomechanically at low temperature before conducting the HRTEM experiments and is referred to as device C in the main text and in table I. The amorphous material visible in Figs. 6 (a) and (c) presumably consists of hydrocarbons adsorbed during their exposure to air and the particle growth [2].

Using such HRTEM images, we determined the number of walls and the associated diameters for six different devices ranging from single wall to seven wall nanotubes. Table II shows the diameters obtained by HRTEM together with other parameters obtained by SEM. The calculation of the Young's modulus in the table is outlined in Section III.

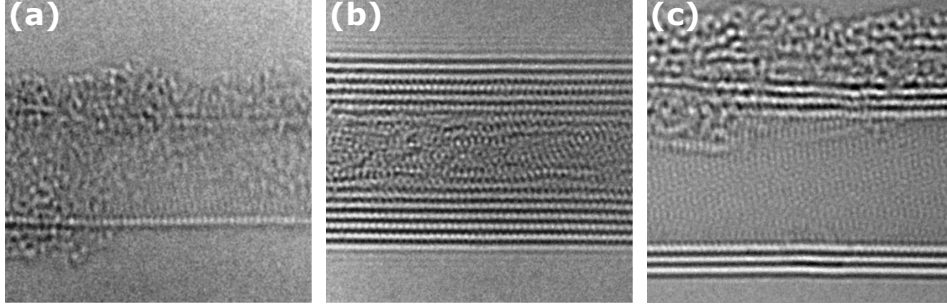


FIG. 6. HRTEM images recorded near the clamping point of single wall device T1 (a), seven wall device T6 (b) and triple wall device C (c). In order to enhance the signal-to-noise ratio multiple images were overlaid and averaged. All image dimensions are 10 nm by 10 nm.

TABLE II. Properties of different nanotube cantilevers functionalized with platinum particles. Cantilever length l and spring constant k were obtained by SEM imaging. Number of walls N and associated diameters d_i were obtained by HRTEM. The Young's modulus Y was calculated as described in section III.

Device	N	l (μm)	k (N/m)	d_i (nm)	Y (TPa)
T1	1	2.8 ± 0.1	$(6.51 \pm 1.53) \times 10^{-7}$	$d_1 = 3.24 \pm 0.14$	1.04 ± 0.49
T2	2	2.2 ± 0.1	$(1.93 \pm 0.42) \times 10^{-6}$	$d_1 = 3.37 \pm 0.16, d_2 = 2.58 \pm 0.16$	0.91 ± 0.46
T3	2	1.8 ± 0.1	$(3.33 \pm 0.52) \times 10^{-6}$	$d_1 = 3.58 \pm 0.11, d_2 = 2.80 \pm 0.09$	0.79 ± 0.34
T4	2	3.8 ± 0.1	$(7.42 \pm 1.73) \times 10^{-7}$	$d_1 = 3.75 \pm 0.19, d_2 = 2.89 \pm 0.22$	1.31 ± 0.64
C	3	2.4 ± 0.1	$(1.64 \pm 0.38) \times 10^{-5}$	$d_1 = 5.84 \pm 0.09, d_2 = 5.15 \pm 0.08, d_3 = 4.38 \pm 0.11$	1.35 ± 0.55
T6	7	7.1 ± 0.1	$(7.36 \pm 1.83) \times 10^{-7}$	$d_1 = 6.24 \pm 0.07, d_2 = 5.55 \pm 0.07, d_3 = 4.88 \pm 0.09,$ $d_4 = 4.20 \pm 0.10, d_5 = 3.53 \pm 0.09, d_6 = 2.88 \pm 0.09,$ $d_7 = 2.15 \pm 0.14$	0.96 ± 0.33

II. EIGENMODES AND SPRING CONSTANT OF A CANTILEVER WITH ADDED MASS AT THE FREE END

A. Model

The Euler-Bernoulli partial differential equation (PDE) that describes the motion $y(x, t)$ of a vibrating beam is

$$\frac{\partial^2 y}{\partial t^2} + \frac{YI}{\rho A} \frac{\partial^4 y}{\partial x^4} = 0. \quad (1)$$

In Eq. 1, Y is the Young's modulus, I is the second moment of the cross-sectional area A , and ρ is the density of the carbon nanotube (CNT) with length l . Solution of Eq. 1 is

$$y(x, t) = \cos \omega_n t [c_1 \cos \alpha_n x + c_2 \sin \alpha_n x + c_3 \cosh \alpha_n x + c_4 \sinh \alpha_n x], \quad (2)$$

with radial frequency $\omega_n = c\alpha_n^2$ and $c = \sqrt{\frac{YI}{\rho A}}$. In Eq. 2, α_n is the wave number whereas c_1, \dots, c_4 are constants that will be determined by satisfying boundary conditions. In the presence of a particle with mass m_{bead} at the free end, the boundary conditions to satisfy become: $y|_{x=0} = \partial y / \partial x|_{x=0} = 0$, and $\partial^2 y / \partial x^2|_{x=l} = 0$, $-YI \frac{\partial^3 y}{\partial x^3}|_{x=l} = m_{bead} c^2 \alpha_n^4 y_{x=l}$ [4], in which the effect of the bead's rotary inertia is neglected. Implementing these conditions in Eq. 2 leads to the following characteristic equation

$$\cos \Omega_n \cosh \Omega_n + 1 + m^* \Omega_n (\sinh \Omega_n \cos \Omega_n - \sin \Omega_n \cosh \Omega_n) = 0, \quad (3)$$

where eigenvalues $\Omega_n = \alpha_n l$ are solutions of Eq.3 with $m^* = m_{bead}/m_{beam}$. The eigenmodes associated with the eigenvalues can then be obtained as

$$\Phi_n(x) = \cos(\Omega_n x) - \cosh(\Omega_n x) - \frac{\cos(\Omega_n) + \cosh(\Omega_n)}{\sin(\Omega_n) + \sinh(\Omega_n)} (\sin(\Omega_n x) - \sinh(\Omega_n x)). \quad (4)$$

Figure 7 shows the variation of the first three eigenfrequencies as a function of m^* . When the ratio between the mass of the bead at the free end and the mass of the beam becomes large, the mode shapes approach those of a beam clamped at one end and hinged at the other. The mode shapes for an increasing m^* are shown in Figs. 8. The profile of the fundamental eigenmode is basically unchanged when increasing m^* , in contrast to what happens for the other eigenmodes.

The equivalent spring constant associated with the free-end CNT deflection for the n -th eigenmode, k_n , can be calculated as follows [5]:

$$k_n = \frac{YI}{l^3} \frac{\int_0^1 (\Phi_n''(x))^2 dx}{\Phi_n(1)^2}. \quad (5)$$

By letting $I = \pi(d^3 g + d g^3)/8$ in Eq. 5, with g and d the thickness and the diameter of the CNT, respectively, the explicit form of k_n becomes

$$k_n = \frac{\pi \Omega_n^3 Y (d^3 g + d g^3)}{64 l^3} \frac{-\Omega_n \cos(2\Omega_n) + \Omega_n \cosh(2\Omega_n) + 4\Omega_n \sin \Omega_n \sinh \Omega_n - 2 \cos \Omega_n \sinh \Omega_n + \sin(2\Omega_n) \cosh^2 \Omega_n}{(\sin \Omega_n \cosh \Omega_n - \cos \Omega_n \sinh \Omega_n)^2} + \frac{2 \cosh \Omega_n (\sin \Omega_n - \cos^2 \Omega_n \sinh \Omega_n)}{(\sin \Omega_n \cosh \Omega_n - \cos \Omega_n \sinh \Omega_n)^2}. \quad (6)$$

The effect of the added particle at the free end of the CNT on the standard deviation equation can be now obtained using the equipartition theorem:

$$\sigma_n^2 = \frac{k_B T}{k_n}. \quad (7)$$

The expression in the special case of $m^* = 0$ reduces to Eq.27 of [6]:

$$\sigma_n^2 = \frac{32 k l^3 T}{\pi Y (d^3 g + d g^3) \Omega_n^4}. \quad (8)$$

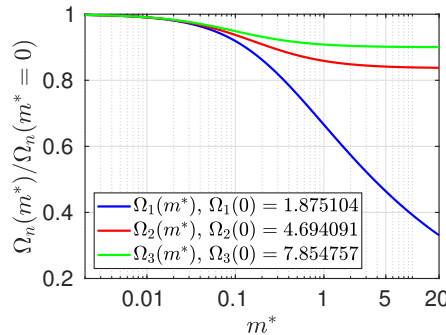


FIG. 7. Influence of m^* on the first three eigenfrequencies of a beam with added mass (m_{bead}) at the free end.

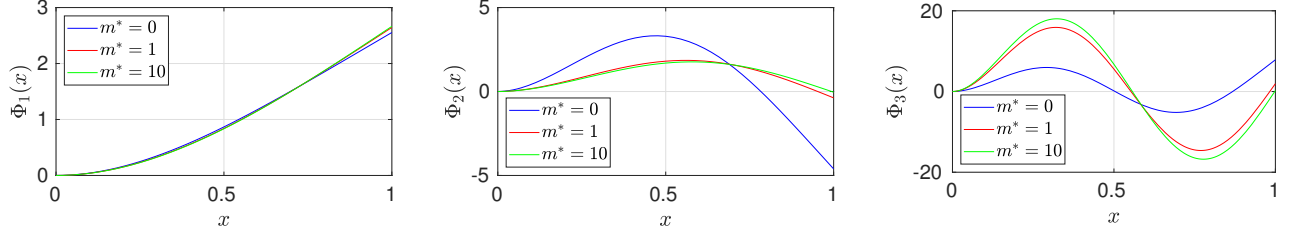


FIG. 8. Influence of m^* on the first three eigenmodes: (a) $\Phi_1(x)$; (b) $\Phi_2(x)$; (c) $\Phi_3(x)$. Functions normalized such that $\int_0^1 \Phi_n(x) dx = 1$.

The resultant standard deviation σ of the cantilever can be obtained by summing up all the independent contributions of eigenmodes. Considering the first 10 flexural modes the expression becomes:

$$\sigma^2 = \sum_{n=1}^{N=10} \sigma_n^2 = 0.84879167978 \frac{k_B l^3 T}{(d^3 g + dg^3) Y}. \quad (9)$$

The numerical coefficient in Eq. 9 is function of the number of modes considered in the summation N and depends on the influence of the added mass. This is illustrated in Figure 9 and reported in Tab. III. The standard deviation of the cantilever is primarily given by that of the fundamental eigenmode independently of the particle mass at the free end.

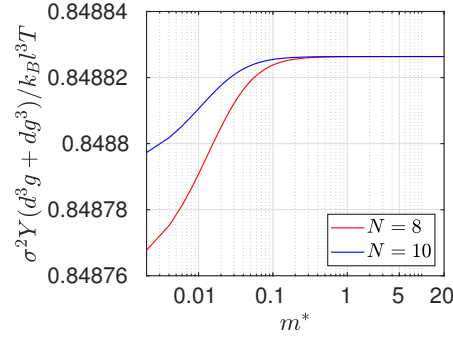


FIG. 9. Variation of the coefficient of Eq. 9 as a function of m^* and while considering a different number of modes N in the summation.

TABLE III. Numerical values for the coefficient of the standard deviation in Eq. 9 when taking into account the fundamental eigenmode only ($N = 1$, middle column) and the first ten eigenmodes ($N = 10$, right column).

m^*	$\sigma_1^2 \frac{Y (d^3 g + dg^3)}{k_B l^3 T}$	$\sum_{n=1}^N \sigma_n^2 \frac{Y (d^3 g + dg^3)}{k_B l^3 T}$
0	0.8239457176	0.8487916797
0.1	0.8363888890	0.8488254732
0.2	0.8414352614	0.8488261068
0.5	0.8462500190	0.8488263184
1	0.8479201355	0.8488263516
2	0.8485513611	0.8488263602
5	0.8487764942	0.8488263627
10	0.8488133432	0.8488263630
20	0.8488230357	0.8488263631

B. Experiment

The model of the previous subsection indicates that the platinum particle does not affect the restoring force nor the eigenmode shape of the two fundamental eigenmodes, which are polarized in perpendicular directions, while the shapes of the higher frequency eigenmodes are strongly modified by the platinum particle. For the higher frequency eigenmodes, the displacement amplitude at the free end is suppressed to zero when the particle has a larger mass than the nanotube. For this reason, our detection method based on the reflection at the free end can only measure the two fundamental modes. This is what we observe in Fig. 10 for device A. The resonances of the fundamental mode doublet are clearly visible, whereas the resonance frequencies of the second bending mode doublet are expected to be about 900 kHz but cannot be detected.

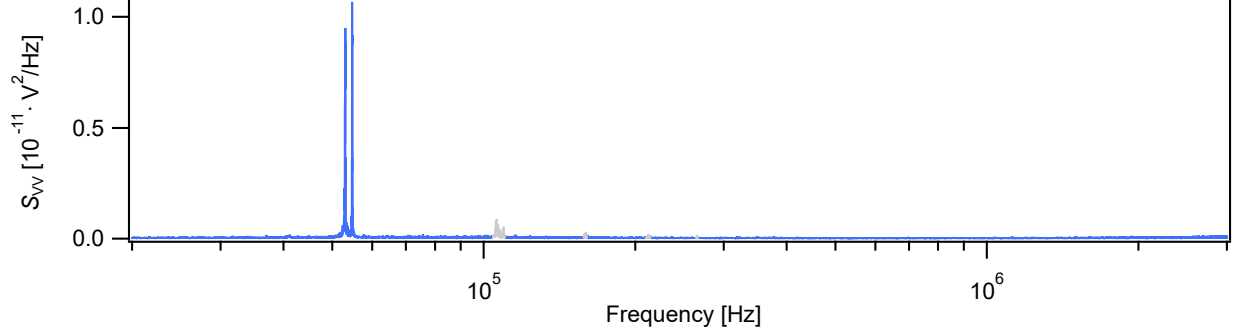


FIG. 10. Power spectrum of the optical reflection from device A undergoing thermal motion at 300 K. The two near-degenerate peaks are associated with the fundamental modes polarized in perpendicular directions. The spectrum is shown over a narrower frequency range in Fig. 1c of the main text. The nonlinearity in the detection results in higher harmonics of these modes, which are marked in gray.

III. ESTIMATION OF Y

We determine the Young's modulus at $T = 300$ K for various nanotube cantilevers. We use the geometrical parameters determined by SEM and HRTEM as described in Sec. I (see table II). The spring stiffness k of a nanotube cantilever composed of N concentric shells is the sum of the spring constant k_i of each shell,

$$k = \sum_{i=1}^N k_i, \quad (10)$$

where we assume that the interaction between the concentric shells has negligible contribution to the spring stiffness. We determine Y of a nanotube cantilever with N shells from its measured spring stiffness, its length, and the diameter d_i of each shell, using

$$Y = 0.8488 \frac{kl^3}{\sum_{i=1}^N (d_i^3 g + g^3 d_i)}, \quad (11)$$

where we assume that all the shells have the same Young's modulus and the wall thickness is $g = 0.34$ nm. This expression can be obtained from Sec II.

Figure 11 shows the resulting Y for the six measured devices plotted as a function of the cantilever length. The error bars represent the standard error ΔY for each measurement, which is determined by expanding Eq. 11 and calculating the propagation of the measurement uncertainties in l , k and d (see table II). The solid line is the mean Young's modulus $\bar{Y} = \sum Y/N = 1.06$ TPa whereas the dashed lines indicate the confidence intervals $\Delta \bar{Y}$. The latter is estimated by summing the standard error of the Y value of the different cantilevers and the mean of their standard error ΔY divided by \sqrt{N} , which yields $\Delta \bar{Y} = \pm 0.28$ TPa.

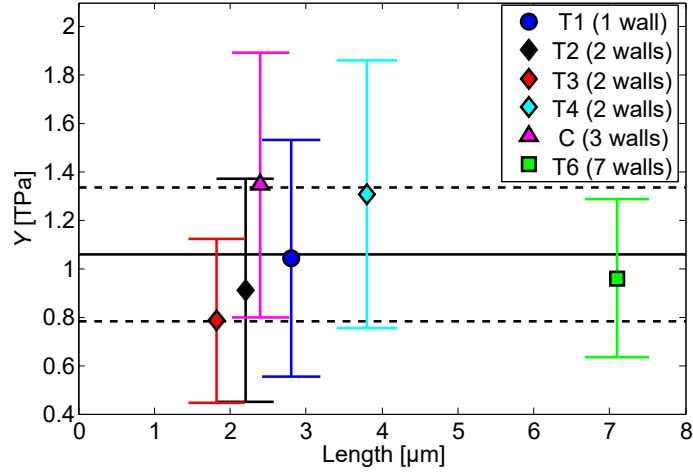


FIG. 11. Y determined from SEM and HRTEM for six different nanotube cantilevers. The error bars represent the standard error for each measurement. The solid black line marks the mean value $\bar{Y} = 1.06$ TPa of all the measurements and the dashed black lines indicate the corresponding confidence intervals $\Delta\bar{Y} = \pm 0.28$ TPa.

IV. DISCUSSION ON THE ORIGIN OF THE TEMPERATURE DEPENDENCE OF THE RESONANCE FREQUENCY

In the main text, we discuss the measured temperature dependence of the resonance frequency in terms of the variation of Y . Here, we consider other possible mechanisms but we show that they cannot account for our measurements.

The measured T dependence of ω_0 could originate from the variation of the mass m adsorbed on the nanotube. However, mass adsorption, which occurs when lowering T , would lead to a reduction of ω_0 [2, 7–9], which is just the opposite of what is measured. Moreover, we do not observe any hysteresis in ω_0 when cooling the device from 300 K to cryogenic temperatures and then heating it back to 300 K, which shows that temperature-induced mass adsorption and desorption plays a negligible role [9]. Thus, the measured variation of $\omega_0(T)$ is not accounted for by adsorbed mass changes.

The measurements could be related to the change in the length of the nanotube when the thermal environment is varied, since the spring constant depends on the nanotube length as $k \propto l^{-3}$. However, the measured resonance frequency reduction at room temperature $\Delta\omega_0(T = 300 \text{ K})/\omega_0 \simeq -2.2 \times 10^{-2}$ for device A is much larger than the predicted reduction $\Delta\omega_0(T = 300 \text{ K})/\omega_0 = -1.25 \times 10^{-3}$ based on the longitudinal expansion of the nanotube in different thermal conditions obtained from our molecular dynamics simulations for a (8,8) CNT. The predicted relative

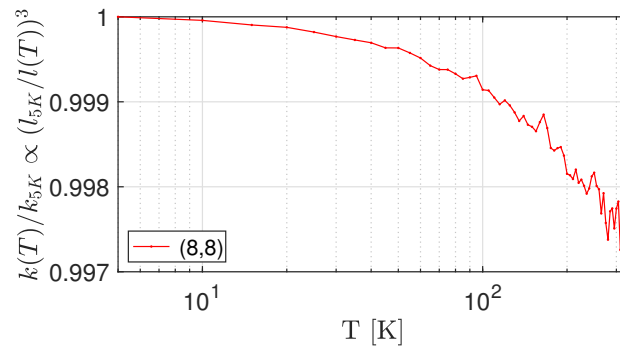


FIG. 12. Predicted relative change in stiffness with respect to temperature induced by the nanotube elongation. MD simulations for a (8,8) CNT fully clamped at one end and free on the other.

change in stiffness $k(T)/k_{5K}$ associated with the thermal expansion of the nanotube as a function of temperature is shown in Fig. 12. The results are obtained by calculating the elongation of the nanotube for different thermalisation temperatures. Here we assume that the stiffness ratio $k(T)/k_{5K}$ is proportional to the cube of the function $(l_{5K}/l(T))$ in which l_{5K} and $l(T)$ are the length of the CNT at 5K and at temperature T , respectively. The decreasing behaviour reported in Fig. 12 suggests that the nanotube stretches with the increase in temperature. Overall, this shows that the thermal expansion is not the cause of the measured $\omega_0(T)$ reduction.

Another possible origin could be the nanotube resonance frequency change that arises from the combination of the Duffing nonlinearity and the thermal motion. Figure 13a shows the measured variation of the resonance frequency as a function of driven vibrational amplitude $\langle x_{\text{vibra}}^2 \rangle$, which allows us to quantify the Duffing constant γ_{eff} using

$$\Delta\omega = \frac{3}{8} \frac{\gamma_{\text{eff}}}{\omega_0} \langle x_{\text{vibra}}^2 \rangle. \quad (12)$$

The driven amplitude is calibrated following the procedure described in Ref. [1]. We compute the linear temperature dependence of the resonance frequency expected from the combination of the Duffing nonlinearity and the thermal vibrations using

$$\Delta\omega = \frac{3}{8} \frac{\gamma_{\text{eff}}}{\omega_0} \langle x_{\text{th}}^2 \rangle = \frac{3}{8} \frac{\gamma_{\text{eff}}}{\omega_0} \frac{k_B T}{k}. \quad (13)$$

Figure 13b shows that the slope of the expected dependence is positive, in contrast to what we measure. Moreover, the frequency shift $\Delta\omega_0(T = 300 \text{ K})/\omega_0 = 3.0 \times 10^{-5}$ is much smaller in magnitude than the measured value $\Delta\omega_0(T = 300 \text{ K})/\omega_0 \simeq -2.2 \times 10^{-2}$. This shows that the Duffing nonlinearity together with the thermal vibrations cannot describe our experimental findings.

Another explanation for our data could be related to the diffusion of adsorbed atoms along the nanotube. Mechanical vibrations lead to a force that pushes atoms towards the anti-node of the mode [10]. Enhancing the vibrational amplitude of the fundamental mode results in more atoms near the nanotube free end and, therefore, a larger effective mass of the mode and a lower resonance frequency. However, we observe the opposite behaviour in Fig. 13a. This shows that the effect of the diffusion of adsorbed atoms is smaller than that of the Duffing nonlinearity, so that it cannot account for the measured T dependence of ω_0 .

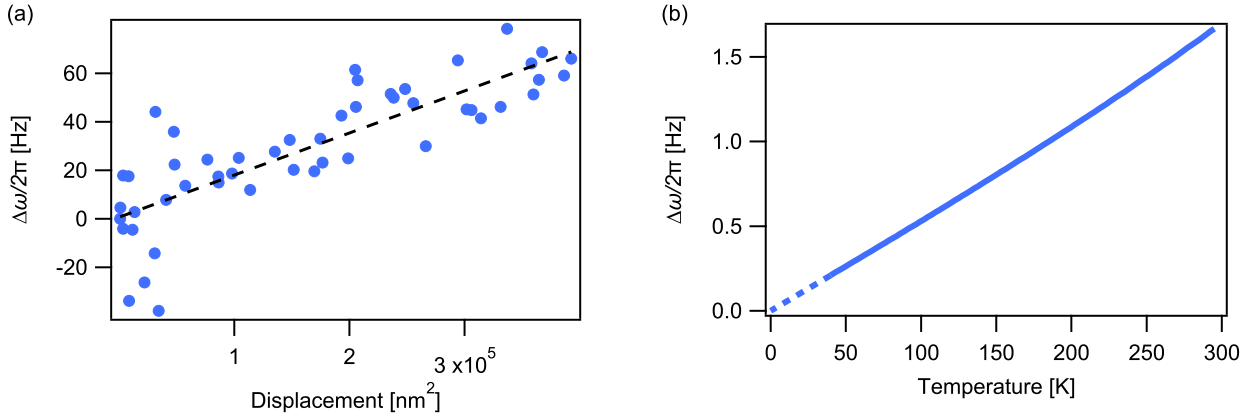


FIG. 13. Estimation of the Duffing constant and its effect on the temperature dependence of the resonance frequency for device A. (a) Variation of the resonance frequency as a function of driven vibrational amplitude measured at $T = 100 \text{ K}$. (b) Estimated frequency shift as a function of temperature due to the Duffing constant and the thermal vibrations.

V. MOLECULAR DYNAMICS SIMULATIONS

We report molecular dynamics simulations of the Brownian motion of carbon nanotubes over a finite temperature range. Simulations are carried out in the Large-scale Atomic/Molecular Massively Parallel Simulator (LAMMPS) software [11] for single layer CNTs of different chirality. In Figure 14 we showcase the geometry of one such CNT.

To account for atom-atom interactions, we use the Tersoff potential [12] with optimized parameters for lattice dynamics and phonon thermal transport [13]. We note that this potential is commonly used for simulating atomic interactions and predicting mechanical properties of carbon-based nanomaterials [14, 15].

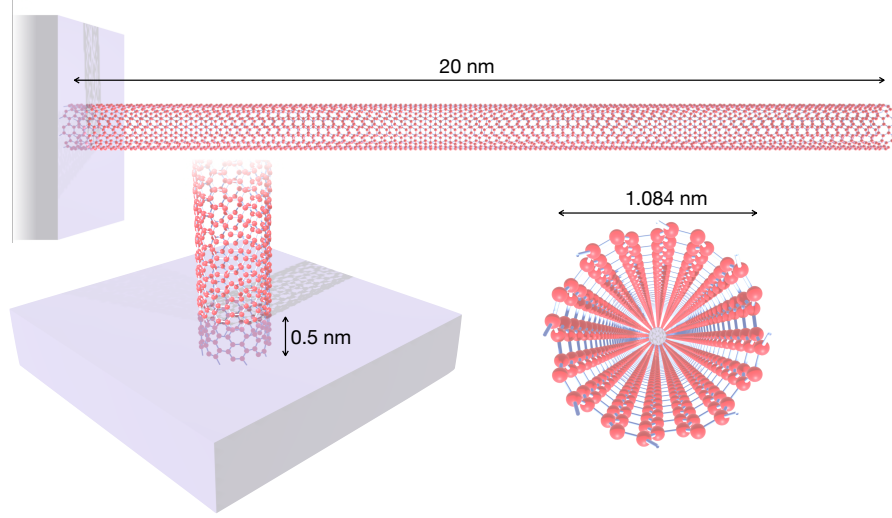


FIG. 14. (8,8) CNT with a total of 2624 atoms. Atoms at one end are clamped for a length of 0.5 nm. The (8,8) CNT has a radius of 0.542 nm and a total length of 20 nm.

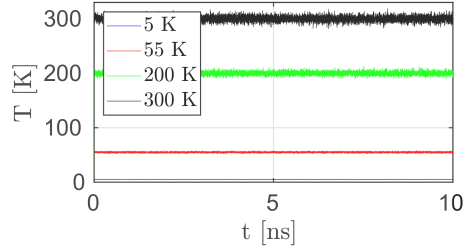


FIG. 15. Temperature fluctuation during the thermalization phase for a (8,8) CNT. For the thermostat temperature of 300 K we obtain a mean of 300.031 K and standard deviation of 5.69 K.

To track the Brownian motion of the nanotube, the system is initially relaxed to ensure equilibrium at the minimum potential state. The minimization of the total potential energy is performed via the Polak-Ribiere conjugate gradient algorithm [16]. The starting point for the minimization procedure is the initial configuration of the atoms, and the potential energy of the system is considered to be in a local minimum when its energy is less than 1×10^{-10} eV or when the forces are less than 1×10^{-10} eV/Å. After the relaxation, at one end, the translational degrees of freedom are constrained for all atoms for a length of 5 nm (see Figure 14). This constraint is applied to obtain a CNT cantilever. Once the equilibrium position is obtained, Newton's equations are integrated using the velocity-Verlet algorithm, with a time-step $dt = 0.1$ fs to determine the variation of the position and velocity of the atoms.

To account for the thermal effects, the system is then equilibrated in a constant volume and temperature ensemble (NVT). The temperature is first brought to a certain value and then kept constant by applying the Nose-Hoover algorithm that thermostats the translational velocity of atoms [17]. The algorithm for the thermalisation is applied for 10 ns to ensure that a stable temperature is obtained (see Fig. 15). Once thermal equilibrium is reached, the vibration response is studied in an energy conserving ensemble (NVE). In this context, the thermal fluctuations of the CNT are monitored for 50 ns discarding an initial transient response of 10 ns, and the coordinates of all atoms are saved every 2.5 ps.

To obtain the resonance frequencies of the CNT, we compute the FFT of the extracted time signals from molecular dynamics. An example of one such FFT averaged over all atoms is shown in Figure 16(a) for a (8,8) CNT at 50 K. The thermal influence on the mechanics of the CNT is obtained by tracking the natural frequencies as a function of the thermostat temperature. The relative change of the square of the frequencies for the first three flexural modes for the (8,8) CNT cantilever is shown in Figure 16(b); this quantity is equal to the relative change of the spring constant $\Delta k(T)/k$. The first three flexural modes highlight the same reduction with respect to the variation of the thermal bath. The staircase behaviour of the first flexural mode is due to the insufficient resolution in frequency (i.e. 20 MHz). Our results are compared to experimental measurements in Fig. 3 of the main text.

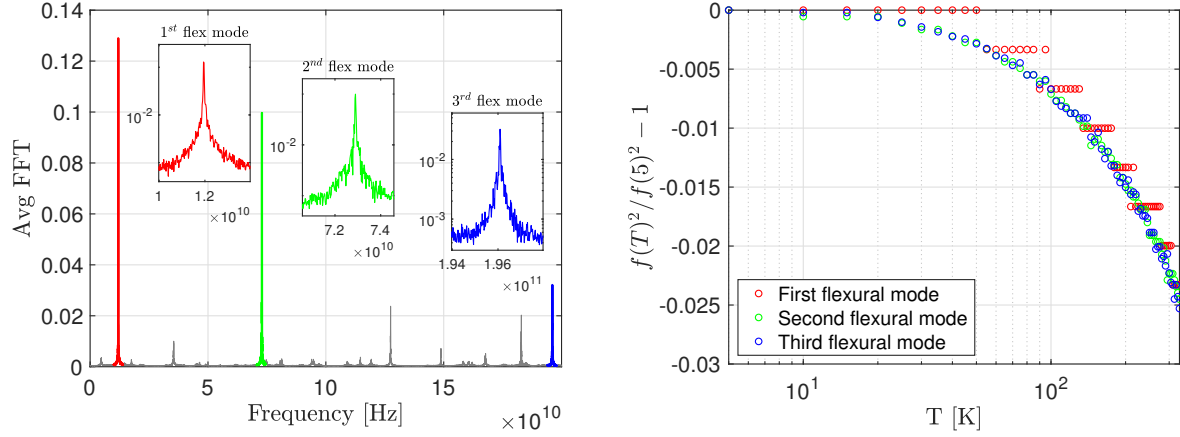


FIG. 16. a) The averaged frequency spectrum of all atoms for the (8,8) CNT at $T = 50$ K. . b) Relative change of the square of frequency with temperature for the first three flexural modes of the CNT from 5K to 330 K with a temperature increment of 5 K. The staircase behaviour of the first flexural mode is due to the insufficient resolution in frequency

We remark that the spectral analysis performed to extract the thermal behaviour of the system, does not allow for an immediate classification of the natural modes of the system and their associated eigenfrequencies. However, it is possible to unravel spatial information of the nanotube from the time response data via the proper orthogonal decomposition (POD) method. The details of this technique can be found in [18] and are briefly described in Sec. V A. Using POD, we can identify the eigenmodes corresponding to the resonance peaks of Figure 16(a). The mode shapes for the first three flexural modes obtained via POD for a (8,8) CNT at 50 K are reported in Figure 17. The procedure outlined above has been repeated in the temperature range $T \in [5, 330]$ K, for three different chiralities namely (5,10), (8,8), and (10,10), and the results are shown in Figure 3(b).

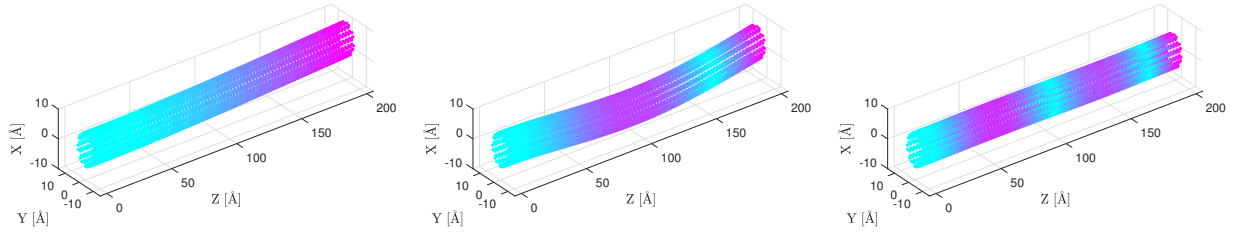


FIG. 17. Mode shapes obtained via proper orthogonal decomposition at $T = 50$ K. (a) First flexural mode. (b) Second flexural mode. (c) Third flexural mode. Modes are amplified ten times for visualization. Colormap for the norm of x and y displacement.

A. Proper orthogonal decomposition

The MD simulations provide the time response in a vector \mathbf{u} comprising the position of M -atoms. The time history consists of N snapshots of the motion as $[\mathbf{u}(t_1), \mathbf{u}(t_2), \dots, \mathbf{u}(t_N)]$. We remove the time average (mean values) of the responses by obtaining the time-varying part, $\mathbf{x}(t_i) = \mathbf{u}(t_i) - \text{mean}(\mathbf{u})$. To extract the proper orthogonal modes of vibrations, a discrete matrix \mathbf{X} is first built such that each row corresponds to a time response of one atom and each column corresponds to a snapshot of the CNT at a specific time as:

$$\mathbf{X} = [\mathbf{x}(t_1) \ \mathbf{x}(t_2) \ \cdots \ \mathbf{x}(t_N)] = \begin{bmatrix} x_1(t_1) & \cdots & x_1(t_N) \\ \vdots & \ddots & \vdots \\ x_M(t_1) & \cdots & x_M(t_N) \end{bmatrix}, \quad (14)$$

where $x_i(t_j)$ is the response of the i -th atom at time t_j . Once matrix \mathbf{X} is constructed, the orthogonal modes are obtained by using the singular-value decomposition (SVD) of the discrete matrix. The SVD operator decomposes \mathbf{X} as:

$$\mathbf{X} = \mathbf{U}\mathbf{\Sigma}\mathbf{V}^*, \quad (15)$$

where \mathbf{U} is an $M \times M$ real or complex unitary matrix, Σ is a $M \times N$ rectangular diagonal matrix with non-negative real diagonals σ_i that are the singular values of \mathbf{X} , and \mathbf{V} is an $N \times N$ real or complex unitary matrix, with \mathbf{V}^* being its conjugate transpose. The columns of \mathbf{U} and \mathbf{V} are the so-called left-singular and right-singular vectors of \mathbf{X} , respectively. Among these matrices, \mathbf{U} corresponds to proper orthogonal modes of vibration that can linearly obtain all the snapshots of the motion with minimum error. Using this matrix we can identify the modes corresponding to the peaks seen in Figure 16 and report them in Figure 17.

VI. QUASI-HARMONIC APPROXIMATION

The elastic constants of a solid are defined as appropriate derivatives of the free energy with respect to strain tensor components [19]. In particular, the Young's modulus of a nanotube along the axial direction can be computed from:

$$Y(T) = \frac{1}{V_0(T)} \left(\frac{\partial^2 F(T, \epsilon)}{\partial \epsilon^2} \right)_{\epsilon=0}, \quad (16)$$

where $F(T, \epsilon)$ is the free energy at temperature T and strain ϵ , and $V_0(T)$ is the equilibrium volume at that temperature. It is frequent to assume that the temperature dependence of elastic constants is small and close to their zero-temperature value, which amounts to substituting the internal energy in place of the free energy in Eq. (16). However, in this work we are particularly interested in the temperature-dependence of the Young's modulus. To this end we resort to a quasi-harmonic approximation of the free energy:

$$F(T, \epsilon) \approx F_0(\epsilon) + F_{vib}(T, \epsilon) = F_0(\epsilon) + k_B T \sum_{n\mathbf{k}} \ln \left[2 \sinh \left(\frac{\hbar \omega_{n\mathbf{k}}(\epsilon)}{2k_B T} \right) \right], \quad (17)$$

where $F_0(\epsilon)$ is the free energy at zero temperature (i.e. the potential energy) at ϵ strain, $\omega_{n\mathbf{k}}(\epsilon)$ is the frequency of vibrational mode n at reciprocal lattice vector \mathbf{k} calculated at strain ϵ . The nanotube phonon frequencies have been calculated using a tight-binding model [20] employing the PHON package [21] (Fig. 18). From the free energy we can obtain the temperature-dependent Young's modulus via Eq. (16). Our results are compared with experimental measurements in Fig. 3 of the main text.

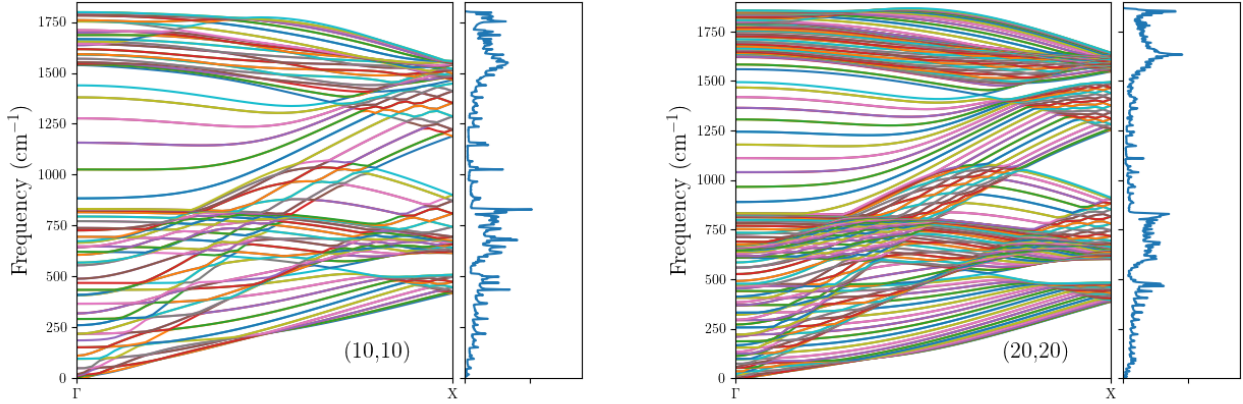


FIG. 18. (a) panel shows the phonon band structure and vibrational density of states for the (10,10) nanotube (see text). (b) panel shows the same information for the (26,0) nanotube.

VII. ESTIMATION OF PHONON DECAY RATES

We estimate the decay rates for different phonon modes using the expressions derived by de Martino et al. [22]. For the longitudinal phonon modes the decay rate due to phonon-phonon interactions is given by

$$\tau_L^{-1} = \frac{\hbar}{4\pi\rho r^4} \left\{ \frac{\sqrt{k_{ph}r}}{2^{5/4}} \coth \left(\frac{\hbar v_L k_{ph}}{4k_B T} \right) + \sqrt{2} \exp \left(\frac{-\hbar v_L}{2\sqrt{2}rk_B T} \right) \sinh \left(\frac{\hbar v_L k_{ph}}{2} \right) \right\} \quad (18)$$

where \hbar is the reduced Planck constant, $\rho = 3.8 \times 10^{-7} \text{ kg/m}^2$, r is the nanotube radius, k_{ph} is the phonon wave number, and $v_L = 1.99 \times 10^4 \text{ m/s}$ is the longitudinal speed of sound. For the twist phonon modes the decay rate is

$$\tau_T^{-1} = \frac{\hbar}{2\rho} \left(\frac{v_T}{v_L} \right)^{7/2} \frac{2^{1/4} (k_{\text{ph}} r)^{3/2}}{8\pi r^4} \left\{ \coth \left(\frac{\hbar v_T k_{\text{ph}}}{4k_B T} \right) + 2^{5/4} \left(\frac{v_T}{v_L k_{\text{ph}} r} \right)^{3/2} \exp \left(-\frac{\hbar v_T^2}{2\sqrt{2} v_L r k_B T} \right) \sinh \left(\frac{\hbar v_T k_{\text{ph}}}{2k_B T} \right) \right\} \quad (19)$$

where $v_T = 1.23 \times 10^4 \text{ m/s}$. We calculate the decay rates for different phonon energies E_{ph} . The wave number is $k = E_{\text{ph}}/\hbar v_L$ for longitudinal and $k = E_{\text{ph}}/\hbar v_T$ for twist phonons and $r = 1 \text{ nm}$. Figs. 19 (a)-(b) show the respective temperature dependencies of τ_L and τ_T .

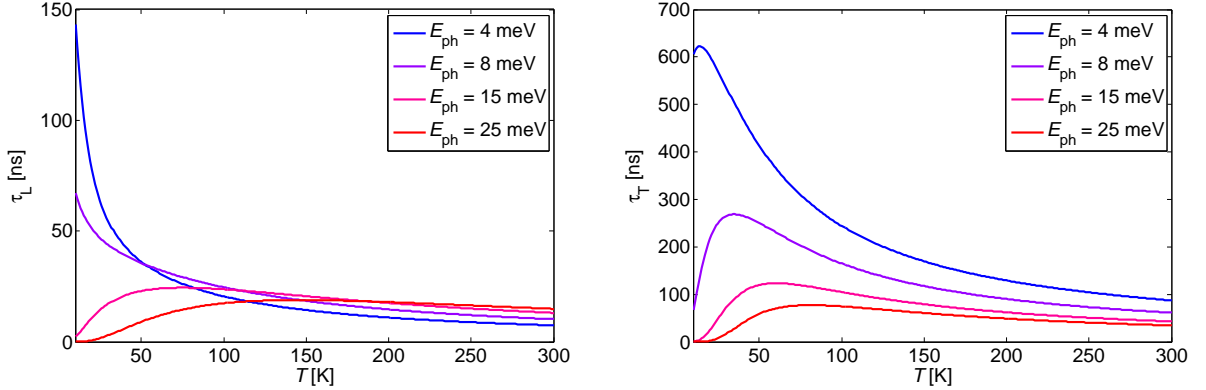


FIG. 19. Temperature dependence of the phonon decay times of the longitudinal (left) and twist phonon modes (right) for different phonon energies E_{ph} .

VIII. AKHIEZER DISSIPATION

The general expression of the Akhiezer dissipation rate Γ_{Akh} of a mechanical eigenmode can be found in Eq. 70 of Ref. [23]. We do not reproduce it here, since the description of the different terms would be rather long. This expression is derived for nonlinear dissipation, but the linear Akhiezer dissipation rate can be obtained from this Eq. 70 when using the proper V_α for the coupling between the mechanical resonator and the high-energy phonon modes.

The temperature enters in Γ_{Akh} through (i) the number of phonon modes with energy $\hbar\omega_k \lesssim k_B T$, (ii) the thermal number \bar{n}_k of quanta for each phonon mode, and (iii) the decay rate $1/\tau_k$ of each phonon mode. When increasing the temperature, the contributions (i) and (ii) enhance Γ_{Akh} , while the contribution (iii) lowers it. Moreover, when the decay rate of a phonon mode is much shorter than the period of the mechanical eigenmode, $\omega_0 \tau_k \gg 1$, this mode does not contribute to Γ_{Akh} . Since the density of states of phonons varies up and down as a function of energy (Fig. 18), it might well happen that Γ_{Akh} depends in a non-monotonic way on temperature, resulting in peaks in dissipation.

IX. DISSIPATION DUE TO DEFECTS

We show in this section that the measured temperature dependence of the dissipation cannot be described by the model that is used in the literature [24, 25] to quantify dissipation due to defects. Peaks in dissipation when sweeping temperature is often attributed to microscopic defects. These defects are modelled by double-well potentials with barrier height V_0 and asymmetry Δ between the two wells. At the high temperature of our experiments, the passage from one well to the other well is thermally activated with a characteristic time

$$\tau_d = \tau_{d0} \exp(V_0/k_B T), \quad (20)$$

with $1/\tau_{d0}$ the attempt rate to overcome the barrier. Assuming that all defects have similar V_0 , Δ , and τ_{d0} , a peak in dissipation occurs when the characteristic rate $1/\tau_d$ of the defects matches the mechanical resonance frequency,

$1/\tau_d = \omega_0$. Our measurements in Fig. 4b of the main text show dissipation peaks at different temperatures. Using the values of these temperatures together with $1/\tau_d = \omega_0$, we construct a plot of τ_d as a function of T (Fig. 20a). Despite the relatively large spread in the values of τ_d in Fig. 20a, the data cannot be described by an exponential behaviour, suggesting that $\exp V_0/k_B T \sim 1$ in the measured temperature range in order to force a reasonable description of the data by Eq. 20. Such an analysis would lead to an unrealistically long $\tau_{d0} \sim 2 \times 10^{-6}$ s, considering that τ_{d0} is typically in the 10^{-13} s – 10^{-11} s range [24–26]. If we were considering two or three different types of defects, each of them with well defined characteristics V_0 , Δ , and τ_{d0} , we would also obtain τ_{d0} in the μ s range. Therefore, the model based on defects with narrow characteristics distribution cannot account for our measurements. Another possibility with the double-well potential model is to assume a broad distribution of the defect characteristics V_0 and Δ [24–26]. A peak in dissipation can be obtained in a specific parameter space region. The peak always features a negative curvature between $T = 0$ K and the peak temperature (Fig. 20b), which is just the opposite of what is observed in our experiments (Fig. 4 of the main text). Overall, our measurements cannot be explained by the double-well potential model with neither a narrow nor a broad defect characteristics distribution.

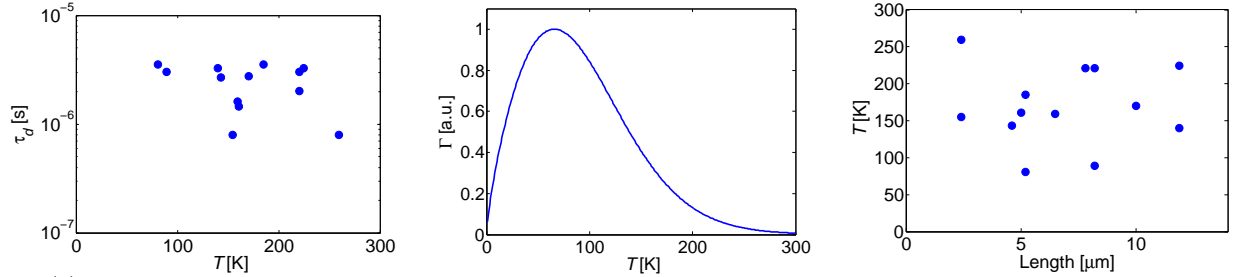


FIG. 20. (a) Characteristic time τ_d to overcome the barrier height as a function of temperature, obtained from all the measured devices as explained in the text. (b) Mechanical dissipation due to a distribution of defects as a function of temperature, calculated using Eq. A1 from reference [26] with $\tau_{d0} = 10^{-12}$ s, $V_0 = 100$ meV, $\Delta = 20$ meV, $\omega_0/2\pi = 100$ kHz and $\zeta = 0.25$. (c) The temperature of the dissipation peaks as a function of the nanotube cantilever length. The data do not indicate any correlation between the dissipation peak temperature and the length. The same is observed for other geometric properties of the nanotubes, such as radius, number of walls, and radius/length ratio (not shown).

-
- [1] A. Tavernarakis, A. Stavrinadis, A. Nowak, I. Tsioutsios, A. Bachtold, and P. Verlot, *Nature Communications* **9**, 662 (2018).
 - [2] G. Gruber, C. Urgell, A. Tavernarakis, A. Stavrinadis, S. Tepsic, C. Magen, S. Sangiao, J. M. De Teresa, P. Verlot, and A. Bachtold, *Nano letters* **19**, 6987 (2019).
 - [3] I. Tsioutsios, A. Tavernarakis, J. Osmond, P. Verlot, and A. Bachtold, *Nano letters* **17**, 1748 (2017).
 - [4] B. Balachandran and E. Magrab, *Vibrations* (Nelson Education, 2008).
 - [5] J. Melcher, S. Hu, and A. Raman, *Applied Physics Letters* **91**, 053101 (2007).
 - [6] A. Krishnan, E. Dujardin, T. W. Ebbesen, P. N. Yianilos, and M. M. J. Treacy, *Physical Review B* **58**, 14013 (1998).
 - [7] Z. Wang, J. Wei, P. Morse, J. G. Dash, O. E. Vilches, and D. H. Cobden, *Science* **327**, 552 (2010).
 - [8] Y. T. Yang, C. Callegari, X. L. Feng, and M. L. Roukes, *Nano Lett* **11**, 1753 (2011).
 - [9] A. Tavernarakis, J. Chaste, A. Eichler, G. Ceballos, M. C. Gordillo, J. Boronat, and A. Bachtold, *PRL* **112**, 196103 (2014).
 - [10] J. Atalaya, A. Isacsson, and M. I. Dykman, *Phys. Rev. Lett.* **106**, 227202 (2011).
 - [11] S. Plimpton, P. Crozier, and A. Thompson, *Sandia National Laboratories* **18**, 43 (2007).
 - [12] J. Tersoff, *Phys. Rev. B* **37**, 6991 (1988).
 - [13] L. Lindsay and D. A. Broido, *Phys. Rev. B* **81**, 205441 (2010).
 - [14] C. Tang, W. Guo, and C. Chen, *Phys. Rev. B* **79**, 155436 (2009).
 - [15] B. I. Yakobson, C. J. Brabec, and J. Bernholc, *Phys. Rev. Lett.* **76**, 2511 (1996).
 - [16] R. Klessig and E. Polak, *SIAM Journal on Control* **10**, 524 (1972).
 - [17] D. J. Evans and B. L. Holian, *The Journal of Chemical Physics* **83**, 4069 (1985).
 - [18] B. Sajadi, S. Wahls, S. van Hemert, P. Belardinelli, P. G. Steeneken, and F. Alijani, *Journal of the Mechanics and Physics of Solids* **122**, 161 (2019).
 - [19] L. Landau and E. Lifshitz, *Theory of Elasticity*, 3rd ed. (Butterworth-Heinemann Ltd., Oxford, 1986).
 - [20] D. Porezag, F. Th., T. Köhler, G. Seifert, and R. Kraschner, *Physical Review B* **51**, 12947 (1995).
 - [21] D. Alfè, *Computer Physics Communications* **180**, 12947 (2009).
 - [22] A. De Martino, R. Egger, and A. O. Gogolin, *Phys. Rev. B* **79**, 205408 (2009).

- [23] J. Atalaya, T. W. Kenny, M. L. Roukes, and M. I. Dykman, [Phys. Rev. B](#) **94**, 195440 (2016).
 - [24] T. Faust, J. Rieger, M. J. Seitner, J. P. Kotthaus, and E. M. Weig, [Phys. Rev. B](#) **89**, 100102 (2014).
 - [25] M. Hamoumi, P. E. Allain, W. Hease, E. Gil-Santos, L. Morgenroth, B. Gérard, A. Lemaître, G. Leo, and I. Favero, [Phys. Rev. Lett.](#) **120**, 223601 (2018).
 - [26] R. Vacher, E. Courtens, and M. Foret, [Phys. Rev. B](#) **72**, 214205 (2005).
-